

Approximate analytical solution for induction heating of solid cylinders



Todd A. Jankowski*, Norma H. Pawley, Lindsey M. Gonzales, Craig A. Ross,
James D. Journey

Los Alamos National Laboratory, P.O. Box 1663, Los Alamos, NM 87545, USA

ARTICLE INFO

Article history:

Received 12 December 2014

Revised 10 August 2015

Accepted 5 October 2015

Available online 20 October 2015

Keywords:

Induction heating

Coupled multiphysics

Perturbation methods

Load signature analysis

ABSTRACT

An approximate solution to the mathematical model for induction heating of a solid cylinder in a cylindrical induction coil is presented here. The coupled multiphysics model includes equations describing the electromagnetic field in the heated object, a heat transfer simulation to determine temperature of the heated object, and an AC circuit simulation of the induction heating power supply. A multiple-scale perturbation method is used to solve the multiphysics model. The approximate analytical solution yields simple closed-form expressions for the electromagnetic field and heat generation rate in the solid cylinder, for the equivalent impedance of the associated tank circuit, and for the frequency response of a variable frequency power supply driving the tank circuit. The solution developed here is validated by comparing predicted power supply frequency to both experimental measurements and calculated values from finite element analysis for heating of graphite cylinders in an induction furnace. The simple expressions from the analytical solution clearly show the functional dependence of the power supply frequency on the material properties of the load and the geometrical characteristics of the furnace installation. The expressions developed here provide physical insight into observations made during load signature analysis of induction heating.

© 2015 The Authors. Published by Elsevier Inc.

This is an open access article under the CC BY-NC-ND license (<http://creativecommons.org/licenses/by-nc-nd/4.0/>).

1. Introduction

Load signature analysis has long been used for process control and monitoring in a variety of induction heating and melting applications [1]. In load signature analysis, electromagnetic observables from the power supply or tank circuit are monitored throughout the induction heating process and are used to infer whether the process will produce an acceptable product. Time-dependent electromagnetic observables include current and voltage, phase angle between current and voltage, and frequency of the applied voltage [1].

As examples, experimental studies have been reported on the use of load signature analysis to improve process control in induction hardening of steel [2,3] and for heating of aluminum plates [4]. Many of these studies use detailed finite element analysis (FEA) of the coupled thermal and electromagnetic problem to quantify changes in the impedance of the tank circuit as the electrical and magnetic properties of the heated material change throughout the heating process [3–6]. These impedance changes throughout the heating cycle are responsible for changing the electromagnetic observables during heating [4]. Although

* Corresponding author. Tel.: +1 505 667 5735; fax: +1 505 665 4631.

E-mail address: jankowski@lanl.gov (T.A. Jankowski).

past load signature analysis studies have used experimental observation and FEA to accurately predict tank circuit impedance change and the corresponding time-evolution of electromagnetic observables during induction heating, the empirical and FEA predictions give little insight into the physical mechanisms responsible for the signatures observed during heating and melting processes. An analytical expression that clearly shows the functional dependence of the impedance on material properties or geometry of the furnace setup is essential for gaining a physical understanding of the observations from load signature analysis.

Load signature analysis is closely related to the more general application of condition monitoring of electrical machines, including motors and generators. In condition monitoring, observable and measureable parameters such as vibration, voltage and/or current spectra, or temperature measurements are used to determine if a piece of machinery is likely to fail and to identify what type of failure is imminent [7–10]. Where load signature analysis uses observables to improve process control, condition monitoring uses observables to detect equipment damage and off-normal conditions.

We presume that techniques drawn from both condition monitoring and load signature analysis can be used in induction heating applications to monitor the heating process and to detect off-normal conditions such as equipment damage (e.g., cracked crucibles, bent work coils) or to identify whether the proper materials or quantities of materials are being heated or melted for a particular application. To establish this diagnostic capability, however, we must first develop a basic physical understanding of the interaction between the power supply and the load and how that interaction affects electromagnetic observables in induction heating applications.

In this paper, we solve the mathematical model describing induction heating of simple non-magnetic cylindrical solids. An approximate perturbation solution for the magnetic field in the cylinder, which is valid provided that the skin depth in the cylinder is smaller than the radius of the cylinder, is formulated. The perturbation solution is used to evaluate a heat source, and the resulting energy equation is solved for the cylinder temperature as a function of time. Finally, a time-harmonic circuit analysis is used to predict the frequency of the voltage-fed power supply throughout cylinder heating. At the outset, the analytical solution for the power supply frequency is shown to be a simple polynomial expression that clearly demonstrates the dependence of the output frequency on the power supply settings, geometry of the coil and load, and material properties of the load. Results are compared to both FEA and experiments.

In Section 2, the mathematical model for the coupled electromagnetic, thermal, and AC circuit simulation is developed and governing equations are presented. In Section 3, approximate solutions to the governing equations for the load temperature and the power supply frequency are developed. The approximate analytical solution is then compared to experimental results obtained during induction heating of graphite cylinders and to an FEA in Section 4. Finally, conclusions are given in Section 5.

2. Model development

A cylinder of radius R and length l is heated by a coil of inside radius b with a number of turns (per unit load length) $n = N/l$. The coil carries a sinusoidal current of frequency f (circular frequency ω) with a peak amplitude I in the circumferential direction. All materials in the model are non-magnetic with permeability $\mu = 4\pi \times 10^{-7}$ H/m. The load (solid cylinder) has electrical conductivity σ , thermal conductivity k , density ρ , and specific heat c . The emissivity of the surface of the cylinder is ε_R . The basic geometry and coordinate system are shown in Fig. 1.

2.1. Equations for electromagnetic field

We assume that the magnetic field will be purely axial, $\mathbf{H} = H\mathbf{e}_z$, while the electric field is purely circumferential, $\mathbf{E} = E\mathbf{e}_\theta$. Therefore, the magnetic and electric fields are fully defined by the scalar quantities H and E , respectively. With these assumptions,

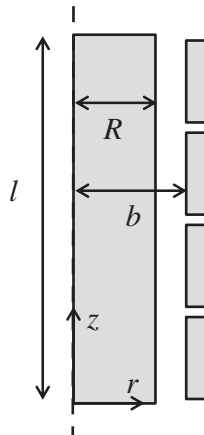


Fig. 1. The geometry and coordinate system used in the induction heating analysis.

the magnetic field in a cylindrical object heated by a close-coupled coil is governed by [11],

$$\frac{d^2 H}{dr^2} + \frac{1}{r} \frac{dH}{dr} - j\omega\mu\sigma H = 0, \quad (1)$$

where $j = \sqrt{-1}$. The electric field in the cylinder can be calculated from,

$$E = -\frac{1}{\sigma} \frac{dH}{dr}. \quad (2)$$

End effects are approximated by imposing an appropriate magnetic field H_s at the outermost surface of the load. The magnetic field is symmetric about the r -axis, and the field is imposed at the surface of the cylinder, or,

$$H(r=R) = H_s \text{ and } \left. \frac{dH}{dr} \right|_{r=0} = 0. \quad (3)$$

The magnetic field at the outermost surface of the load, H_s is set equal to the magnetic field in the gap between the coil and the load [11]. For a short cylindrical current sheet we find,

$$H_s = nIK_n, \quad (4)$$

where nI is the magnetic field for an infinitely long air-filled solenoid and K_n is the modified Nagaoka coefficient to correct for a finite-length coil with a workpiece. The coefficient is evaluated from [12], namely,

$$K_n = \tilde{K}_n \left(1 - \frac{R^2}{b^2} \right) + \frac{R^2}{b^2}, \quad (5)$$

where \tilde{K}_n is the Nagaoka coefficient for a finite-length coil with an air core, which can be estimated from [13],

$$\tilde{K}_n = \frac{1 + 1.535604\beta^2 + 0.273728\beta^4}{1 + 1.035808\beta^2} - \frac{8\beta}{3\pi}, \quad (6)$$

with $\beta = b/l$. The expression in Eq. (6) is valid provided that the length of the coil is larger than the diameter, or $2\beta \leq 1$.

The definition of the skin depth, $\delta = \sqrt{2/(\omega\mu\sigma)}$, along with the dimensionless variables $H^* = H/H_s$, $\eta = r/R$, and $\varepsilon = \delta/R$ are used to write,

$$\frac{d^2 H^*}{d\eta^2} + \frac{1}{\eta} \frac{dH^*}{d\eta} - j \frac{2}{\varepsilon^2} H^* = 0; \text{ with } H^*(\eta=1) = 1 \text{ and } \left. \frac{dH^*}{d\eta} \right|_{\eta=0} = 0. \quad (7)$$

An exact solution to Eq. (7), where the magnetic field is represented by Bessel functions, is well documented for induction heating of cylinders [11]. However, manipulation of the resulting exact solution with Bessel functions to determine the heat generation rate in the cylinder and to solve for the temperature profile is tedious. Moreover, determining functional relationships (i.e. dependence of operating frequency of the power supply, impedance of the tank circuit, etc. on electrical conductivity, geometry, etc.) from the complicated expressions that accompany the exact solution is difficult. We aim here to develop simple expressions, valid for small ε , where the functional dependence of the solution on the geometry and material properties is easily visible.

2.2. Perturbation solution for magnetic field

We aim to find a solution to Eq. (7) that becomes exact as $\varepsilon \rightarrow 0$. A multiple-scale analysis is used to solve the problem [14]. First, we define the outer and inner scales as,

$$\eta = \eta \text{ and } \chi = \frac{1-\eta}{\varepsilon}. \quad (8)$$

Now with $H^* = H^*(\eta, \chi)$, defining a perturbation expansion of the dimensionless magnetic field as,

$$H^* = H_0^* + \varepsilon H_1^* + O(\varepsilon^2), \quad (9)$$

and substituting Eqs. (8) and (9) into Eq. (7) gives,

$$\frac{\partial^2 H_0^*}{\partial \chi^2} - j2H_0^* + \varepsilon \left(\frac{\partial^2 H_1^*}{\partial \chi^2} - j2H_1^* - 2 \frac{\partial^2 H_0^*}{\partial \eta \partial \chi} - \frac{1}{\eta} \frac{\partial H_0^*}{\partial \chi} \right) + O(\varepsilon^2) = 0. \quad (10)$$

The leading order, $O(1)$, equation is solved by,

$$H_0^* = A_1 \exp[(1+j)\chi] + A_2 \exp[-(1+j)\chi], \quad (11)$$

where A_1 and A_2 are functions of η . The $O(\varepsilon)$ equation is,

$$\frac{\partial^2 H_1^*}{\partial \chi^2} - j2H_1^* = 2 \frac{\partial^2 H_0^*}{\partial \eta \partial \chi} + \frac{1}{\eta} \frac{\partial H_0^*}{\partial \chi}. \quad (12)$$

Using Eq. (11) to evaluate the right hand side of Eq. (12), secular terms can be prevented by forcing,

$$dA_1/d\eta = -A_1/2\eta \text{ and } dA_2/d\eta = -A_2/2\eta. \quad (13)$$

Solutions to Eq. (13) yield,

$$A_1 = C_1/\sqrt{\eta} \text{ and } A_2 = C_2/\sqrt{\eta}, \quad (14)$$

where C_1 and C_2 are constants. With Eqs. (11) and (14), the centerline slope and specified magnetic field conditions are satisfied by setting $C_1 = 0$ and $C_2 = 1$. The leading order solution for the magnetic field is then expressed as,

$$H^* = \frac{1}{\sqrt{\eta}} \exp(-\chi)(\cos \chi - j \sin \chi) + O(\varepsilon). \quad (15)$$

2.3. The Poynting vector

Eqs. (2) and (15) can be manipulated to evaluate the electric field in the cylinder. The (dimensional) electric field at the surface of the cylinder $E_s = E(\eta = 1, \chi = 0)$ is evaluated as,

$$E_s = \frac{H_s}{\sigma R \varepsilon} [(\varepsilon/2 - 1) - j] + O(\varepsilon). \quad (16)$$

The power flow (power per unit surface area [W/m²]) into the load is evaluated with the help of the Poynting vector,

$$\mathbf{P} = (\mathbf{E} \times \mathbf{H})_{\eta=1, \chi=0} = P(-\mathbf{e}_r) = -E_s H_s (-\mathbf{e}_r). \quad (17)$$

Using Eq. (4), the surface power flux into the load in the (negative) r - direction is

$$P = \frac{n^2 I^2}{\sigma R \varepsilon} K_n^2 [(1 - \varepsilon/2) + j] + O(\varepsilon). \quad (18)$$

The surface power flux in Eq. (18) is developed using only the leading order solution, $O(\varepsilon)$, for the magnetic field. The solution can easily be extended to higher order by including more terms in the perturbation expansion to Eq. (9). By solving for the next term in the series, the Poynting vector, to $O(\varepsilon^2)$, may be expressed as,

$$P = \frac{n^2 I^2}{\sigma R \varepsilon} K_n^2 \left[(1 - \varepsilon/2 - \varepsilon^2/16) + j(1 + \varepsilon^2/16) \right] + O(\varepsilon^2). \quad (19)$$

These approximate expressions for the Poynting vector are compared to the exact solution given by Davies [11]. The exact solution is reported as,

$$P = \frac{n^2 I^2}{\sigma R \varepsilon^2} K_n^2 [p_d + jq_d], \quad (20)$$

where for the exact solution, p_d and q_d are,

$$p_d = \sqrt{2}\varepsilon \frac{\text{ber}\left(\frac{\sqrt{2}}{\varepsilon}\right)\text{ber}'\left(\frac{\sqrt{2}}{\varepsilon}\right) + \text{bei}\left(\frac{\sqrt{2}}{\varepsilon}\right)\text{bei}'\left(\frac{\sqrt{2}}{\varepsilon}\right)}{\text{ber}^2\left(\frac{\sqrt{2}}{\varepsilon}\right) + \text{bei}^2\left(\frac{\sqrt{2}}{\varepsilon}\right)}, \quad (21)$$

$$q_d = \sqrt{2}\varepsilon \frac{\text{ber}\left(\frac{\sqrt{2}}{\varepsilon}\right)\text{bei}'\left(\frac{\sqrt{2}}{\varepsilon}\right) - \text{bei}\left(\frac{\sqrt{2}}{\varepsilon}\right)\text{ber}'\left(\frac{\sqrt{2}}{\varepsilon}\right)}{\text{ber}^2\left(\frac{\sqrt{2}}{\varepsilon}\right) + \text{bei}^2\left(\frac{\sqrt{2}}{\varepsilon}\right)}, \quad (22)$$

where the functions ber and bei are the Kelvin functions. These expressions from the exact solution are compared to the following expressions, from Eqs. (18) and (19), for the leading order, $O(\varepsilon)$, and high order, $O(\varepsilon^2)$, perturbation solutions. For $O(\varepsilon)$:

$$p_d = \varepsilon - \varepsilon^2/2, \quad (23)$$

and

$$q_d = \varepsilon. \quad (24)$$

For $O(\varepsilon^2)$:

$$p_d = \varepsilon - \varepsilon^2/2 - \varepsilon^3/16, \quad (25)$$

and

$$q_d = \varepsilon + \varepsilon^3/16. \quad (26)$$

The comparisons between the real and imaginary parts of the Poynting vector from the approximate and exact solutions are shown in Table 1 for $0 \leq \varepsilon \leq 1$. The table shows that, especially for the real power deposited in the load p_d , the error between the

Table 1

Real and imaginary parts of the Poynting vector for the exact and multiple-scales solutions.

ε	p_d exact	p_d $O(\varepsilon)$	% error p_d $O(\varepsilon)$	p_d $O(\varepsilon^2)$	% error p_d $O(\varepsilon^2)$	q_d exact	q_d $O(\varepsilon)$	% error q_d $O(\varepsilon)$	q_d $O(\varepsilon^2)$	% error q_d $O(\varepsilon^2)$
0.05	0.049	0.049	0.0	0.049	0.0	0.050	0.050	0.0	0.050	0.0
0.1	0.095	0.095	0.1	0.095	0.0	0.100	0.100	0.1	0.100	0.0
0.2	0.180	0.180	0.3	0.180	0.0	0.201	0.200	0.3	0.201	0.1
0.3	0.254	0.255	0.4	0.253	0.3	0.301	0.300	0.4	0.302	0.1
0.4	0.323	0.320	1.0	0.316	2.2	0.410	0.400	2.3	0.404	1.4
0.5	0.369	0.375	1.5	0.367	0.6	0.537	0.500	6.8	0.508	5.4
0.6	0.375	0.420	12.1	0.407	8.5	0.664	0.600	9.6	0.614	7.5
0.7	0.348	0.455	30.9	0.434	24.7	0.768	0.700	8.8	0.721	6.0
0.8	0.306	0.480	56.9	0.448	46.4	0.842	0.800	5.0	0.832	1.2
0.9	0.263	0.495	88.2	0.449	70.9	0.892	0.900	0.8	0.946	6.0
1	0.224	0.500	122.8	0.438	95.0	0.926	1.000	8.0	1.063	14.8

exact and approximate solutions rises to high levels as ε increases above 0.5. Below $\varepsilon = 0.5$, however, errors are small. Moreover, the table shows that, for small ε , there is only a small difference between the $O(\varepsilon)$ and $O(\varepsilon^2)$ solutions. For this reason, we use the $O(\varepsilon)$ solution throughout the rest of this work and set,

$$P = \frac{n^2 l^2}{\sigma R \varepsilon} K_n^2 [(1 - \varepsilon/2) + j]. \quad (27)$$

As shown in Table 1, this solution is sufficiently accurate provided that $\varepsilon \leq 0.5$.

2.4. Equation for temperature of the load

The energy equation is solved to determine the temperature, T , of the load. The load is assumed to gain energy at the outermost surface due to the eddy currents generated by induction and it is assumed to lose energy by radiation heat transfer from the outermost surface and the top and bottom surfaces.

To simplify the problem, we assume that the thermal conductivity of the load is large enough that a lumped-parameter model can be used. In the lumped parameter model, spatial temperature gradients are ignored, and the cylinder being heated is assumed to attain a uniform temperature spatially at each point in time.

The energy equation for a lumped mass is,

$$\rho c \pi R^2 l \frac{dT}{dt} = q - 2\pi R l \left(1 + \frac{R}{l}\right) \varepsilon_R \sigma_B (T^4 - T_\infty^4), \quad (28)$$

with

$$T(0) = T_\infty, \quad (29)$$

where T_∞ is the ambient temperature and σ_B is the Stefan–Boltzmann constant. The heat transfer rate, q , is evaluated from Eq. (27). The total heat flux (heat transfer rate per unit area) at any point in time to the cylinder is evaluated by averaging the real part of the Poynting vector over one cycle. This gives,

$$q'' = \frac{1}{2} \text{Re}(P) = \frac{n^2 l^2}{2\sigma R \varepsilon} K_n^2 (1 - \varepsilon/2). \quad (30)$$

Then the total heat transfer rate to the outermost surface becomes,

$$q = q'' 2\pi R l = \frac{\pi n^2 l^2}{\sigma \varepsilon} K_n^2 (1 - \varepsilon/2). \quad (31)$$

To simplify the energy equation the following dimensionless variables are defined as,

$$\begin{aligned} \theta &= \frac{T}{T_\infty}, \quad \tau = \frac{t \sigma_B T_\infty^3}{(\rho c)_\infty R}, \quad \sigma^* = \frac{\sigma \sigma_B R T_\infty^4}{n^2 l^2 K_n^2}, \\ \omega^* &= \frac{\omega \mu R n^2 l^2 K_n^2}{2 \sigma_B T_\infty^4}, \quad C_p^* = (\rho c)/(\rho c)_\infty, \end{aligned} \quad (32)$$

where $(\rho c)_\infty$ is the heat capacity of the load evaluated at the (constant) ambient temperature. With this choice, one can substitute into the definition of the skin depth to find that,

$$\varepsilon = \frac{1}{\sqrt{\omega^* \sigma^*}}. \quad (33)$$

Using Eqs. (31)–(33) in Eq. (28) we get,

$$C_p^* \frac{d\theta}{d\tau} = \frac{1}{\sigma^*} \left(\sqrt{\sigma^* \omega^*} - \frac{1}{2} \right) - 2\varepsilon_R \left(1 + \frac{R}{l} \right) (\theta^4 - 1), \quad (34)$$

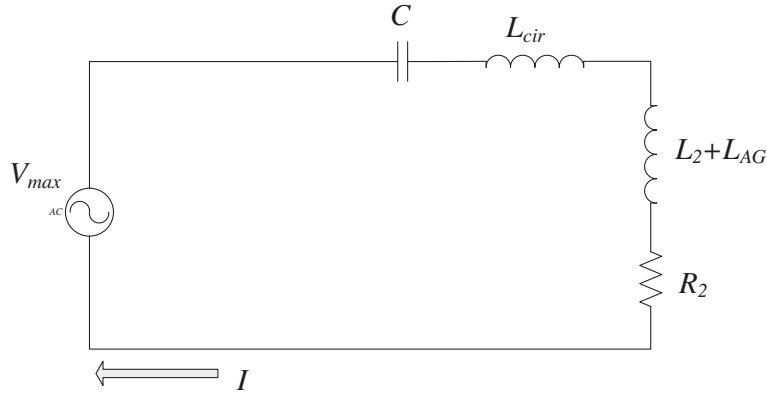


Fig. 2. Diagram of the series tuned tank circuit in current control.

with

$$\theta(\tau = 0) = 1. \quad (35)$$

2.5. Circuit parameters

We next model the power supply to determine the operating frequency. We assume that a series resonant voltage source converter is used and that control is achieved by controlling the frequency of the inverter [15]. This type of voltage-fed inverter was used in the validation experiments described in subsequent sections of this paper. The power supply is used in current control mode, where the output frequency of the power supply, and consequently the equivalent impedance of the tank circuit, is adjusted so that the magnitude of the current drawn by the tank circuit is constant. A diagram of the tank circuit is shown in Fig. 2. The current is fed through a matching capacitor with constant capacitance C . The load impedance is represented as a load resistance R_2 in series with the load inductance $L_2 + L_{AG}$, where L_2 is the component of reactance due to coupling with the load and L_{AG} is the constant inductance of the air gap between the load and the coil. We ignore the resistance of the conductors between the power supply and the coil, while the inductance of the conductors is represented by the constant inductance L_{cir} . Evaluating the magnitude of the total impedance connected to the power supply gives,

$$|Z_{tot}| = \sqrt{R_2^2 + \left[\omega(L_2 + L_{AG} + L_{cir}) - \frac{1}{\omega C} \right]^2}. \quad (36)$$

This impedance magnitude is set equal to the impedance required to draw the set point current I from the power supply with the voltage across the power supply V_{max} . We define the constant $Z_{set} = V_{max}/I$. Setting $|Z_{tot}| = Z_{set}$, defining dimensionless variables for impedance (resistance), inductance, and capacitance as,

$$Z^* = \frac{ZI^2}{\sigma_B R I_\infty^4}, \quad L^* = \frac{2L}{\mu n^2 R^2 I K_n^2}, \quad \text{and} \quad C^* = \frac{2C \sigma_B^2 I_\infty^8}{\mu n^2 I^4 K_n^2}, \quad (37)$$

solving Eq. (36) for the frequency, and keeping only the positive root (since these power supplies typically control above the resonant frequency to protect the switches), yields

$$\omega^* = \frac{\sqrt{Z_{set}^{*2} - R_2^{*2}} + \sqrt{Z_{set}^{*2} - R_2^{*2} + 4(I_2^* + L_{AG}^* + L_{cir}^*)/C^*}}{2(I_2^* + L_{AG}^* + L_{cir}^*)}. \quad (38)$$

The frequency as a function of time is evaluated by substituting expressions for R_2^* , L_2^* , L_{cir}^* and L_{AG}^* into Eq. (38). The inductance of the air gap can be evaluated by using the formula for the self-inductance of a short air-filled solenoid [16],

$$L_{AG} = \mu n l A \frac{dH_s/dt}{dI/dt} = \mu n^2 l A K_n. \quad (39)$$

where A is the cross-sectional area of air. For the air gap in Fig. 1, $A = \pi R^2(b^2/R^2 - 1)$. Substituting, the dimensionless air gap inductance becomes,

$$L_{AG}^* = \frac{2\pi}{K_n} \left[\beta^2 \left(\frac{l}{R} \right)^2 - 1 \right]. \quad (40)$$

To evaluate R_2^* and L_2^* , which are both associated with power absorbed by the load, we first evaluate the impedance of the load. We can write,

$$Z_2 = R_2 + j\omega L_2 = \frac{2\pi R I P}{I^2}. \quad (41)$$

Evaluating P from Eq. (27), and making all parameters dimensionless we have,

$$R_2^* = \frac{2\pi}{\sigma^*} \left(\sqrt{\sigma^* \omega^*} - \frac{1}{2} \right) \text{ and } L_2^* = \frac{2\pi}{\sqrt{\sigma^* \omega^*}}. \quad (42)$$

3. Approximate solutions for load temperature and power supply frequency

3.1. Approximate solution to the energy equation

The temperature of the load is calculated here from Eqs. (34) and (35) using a first order fully explicit integration method. The load temperature is approximated as,

$$\theta_{i+1} = \theta_i + \frac{\Delta\tau}{C_{p,i}^*} \left[\frac{1}{\sigma_i^*} \left(\sqrt{\sigma_i^* \omega_i^*} - \frac{1}{2} \right) - 2\varepsilon_R \left(1 + \frac{R}{l} \right) (\theta_i^4 - 1) \right], \quad (43)$$

where the subscript i refers to a point in time and $\Delta\tau$ is a fixed dimensionless time step. Eq. (43) allows us to start from a specified initial temperature $\theta_0 = 1$ and march through time to calculate the load temperature as heating occurs.

3.2. Approximate solution for power supply frequency

To develop an approximate solution to Eq. (38), first express R_2^* and L_2^* as functions of ε and ω^* . These become

$$R_2^* = 2\pi \omega^* \left(\varepsilon - \frac{1}{2} \varepsilon^2 \right) \text{ and } L_2^* = 2\pi \varepsilon. \quad (44)$$

Next, we recognize that the only parameters varying as functions of time in Eq. (38) are R_2^* and L_2^* , all other parameters are constant. Moreover, Eq. (44) demonstrates that both the load resistance and inductance are small parameters of $O(\varepsilon)$ or higher. To begin, we use the first two terms of the binomial expansions to write,

$$\sqrt{Z_{set}^{*2} - R_2^{*2}} = Z_{set}^* - \frac{1}{2} \frac{R_2^{*2}}{Z_{set}^*}, \quad (45)$$

$$\sqrt{Z_{set}^{*2} - R_2^{*2} + 4 \frac{(L_{AG}^* + L_{cir}^*)}{C^*}} = \sqrt{Z_{set}^{*2} + 4 \frac{(L_{AG}^* + L_{cir}^*)}{C^*}} + \frac{1}{2} \frac{(4L_2^{*2}/C^* - R_2^{*2})}{\sqrt{Z_{set}^{*2} + 4(L_{AG}^* + L_{cir}^*)/C^*}}. \quad (46)$$

Taking Eqs. (44)–(46), and substituting along with the regular perturbation,

$$\omega^* = \omega_0^* + \varepsilon \omega_1^* + \varepsilon^2 \omega_2^* + O(\varepsilon^3), \quad (47)$$

into Eq. (38), the leading order solution is extracted, namely,

$$\omega_0^* = \frac{Z_{set}^*}{2(L_{AG}^* + L_{cir}^*)} \left[1 + \sqrt{1 + \frac{4(L_{AG}^* + L_{cir}^*)}{C^* Z_{set}^{*2}}} \right]. \quad (48)$$

Notice that the expression for the leading order solution is a constant (not a function of time or temperature). In a similar way, equations can be written with terms of $O(\varepsilon)$ and $O(\varepsilon^2)$ to obtain expressions for ω_1^* and ω_2^* . These yield,

$$\omega_1^* = -\frac{2\pi}{(L_{AG}^* + L_{cir}^*)} \omega_0^* + \frac{2\pi}{[2C^*(L_{AG}^* + L_{cir}^*)^2 \omega_0^* - C^* Z_{set}^* (L_{AG}^* + L_{cir}^*)]}, \quad (49)$$

$$\omega_2^* = -\frac{2\pi}{(L_{AG}^* + L_{cir}^*)} \omega_1^* - \frac{\pi^2 \omega_0^{*2}}{Z_{set}^* (L_{AG}^* + L_{cir}^*)} - \frac{\pi^2 \omega_0^{*2}}{[2(L_{AG}^* + L_{cir}^*)^2 \omega_0^* - Z_{set}^* (L_{AG}^* + L_{cir}^*)]}. \quad (50)$$

Again, notice that ω_1^* and ω_2^* are also constants. All of the temperature (and time) dependence is forced into the ε and ε^2 coefficients multiplying the terms in Eq. (47). Finally, we can approximate Eq. (33) as $\varepsilon = 1/\sqrt{\omega_0^* \sigma^*}$, and substitute into Eq. (47) to retrieve an approximate solution for the operating frequency,

$$\omega^* = \omega_0^* + \frac{\omega_1^*}{\sqrt{\omega_0^*}} \frac{1}{\sqrt{\sigma^*}} + \frac{\omega_2^*}{\omega_0^*} \frac{1}{\sigma^*}, \quad (51)$$

where $\sigma^* = \sigma^*(\theta)$. Eqs. (48)–(51) define the approximate solution for the dimensionless frequency output of the power supply.

In the approximate perturbation solution, the power supply output frequency Eq. (51) is represented as a constant, ω_0 , plus small corrections. The constants, ω_0 , ω_1 , and ω_2 depend on the (constant) power supply settings and the geometry of the furnace setup. The time and temperature dependence of the output frequency is shown to be only due to the temperature dependence of the electrical conductivity of the load σ^* . The temperature is solved for by marching in time from the known initial temperature using Eq. (43). Power supply output frequency and load temperature from the analytical model are compared to FEA and experiments in the next section.

4. Model validation: comparisons to finite element analysis and experiments

4.1. Finite element analysis

A number of studies have established methods for using the finite element method to solve and optimize the coupled multiphysics induction heating problem [17–19]. Using these methods, an independent FEA simulation in Comsol Multiphysics has been performed. The two-dimensional, axisymmetric simulation includes an 11-turn induction coil with a solid cylinder as a load. The geometry simulated in Comsol is shown in Fig. 3.

The Comsol simulation includes a frequency domain magnetic field simulation at each point in time of the transient solution. Given the geometry of the furnace, the material properties of the load, and the magnitude and frequency of the current in the coil, Comsol solves for the magnetic vector potential, which is then used to calculate the magnetic and electric fields and the heat generation rates in the load. The frequency of the coil current is determined in Comsol by solving Eq. (38) at each point in time as a user defined equation. The heat generation rate at each point in time is then transferred to a transient heat conduction model, where the transient temperature of the load is estimated. The heat conduction model includes surface-to-ambient radiation heat transfer boundary conditions on all external surfaces of the load. All relevant material properties of the load can be specified as temperature dependent properties. The mesh shown in Fig. 3 was used throughout the simulations. The mesh used allows for a minimum of three elements in the skin depth for all results reported here. Additionally, a mesh resolution study showed that by increasing the number of elements to 1.6 times the number of elements in Fig. 3, the total energy deposited in the load throughout heating was changed by less than 0.01% for all of the results reported here.

4.2. Experimental setup

The induction heating power supply used for the experiments was the Inductoheat SP16. This power supply uses a voltage-fed inverter with power controlled by the operating frequency. The maximum output frequency of the series-tuned power supply is 20 kHz. Tuning capacitance was set to either 15.41 μF or 55.7 μF to observe the effect of frequency changes (skin depth changes) on the heating rates. Experiments were performed in the current control mode. The maximum output current of the power supply (at the primary of the isolation transformer) is limited to 125 A (RMS). The turns ratio of the isolation transformer was set to 17:2. The maximum output voltage of the power supply (at the primary of the isolation transformer) is limited to 400 V (RMS).

A picture of the experimental setup is shown in Fig. 4. The power supply is connected to the induction coil with copper tubing to form the conductors. The 11 turn induction coil is wound from 1.27 cm outside diameter 0.165 cm wall thickness copper tubing with a pitch of 1.75 cm to form a coil with an inside diameter of 13.3 cm. The conductors are a pair of (nominally) 45.7 cm long sections of 0.953 cm outside diameter 0.089 cm wall thickness copper tubes separated by a (nominal) distance of 20.3 cm in series with a pair of 20.3 cm long, 1.27 cm outside diameter 0.165 cm wall thickness copper tubes separated by a distance of 15.2 cm. Based on this geometry, we estimate the inductance of conductors between the power supply and coil to be $L_{\text{cir}} = 0.87 \mu\text{H}$ [16]. The graphite cylinder is a 9.02 cm diameter 19.8 cm long solid graphite cylinder that is centered both radially and axially in the induction coil. The tubing forming the conductors and the coil are water cooled.

Output current was measured on the conductor between the isolation transformer and the induction coil using a Pearson clamp-on current probe, Model 3525. The output frequency was extracted from the output current measurement. Cylinder

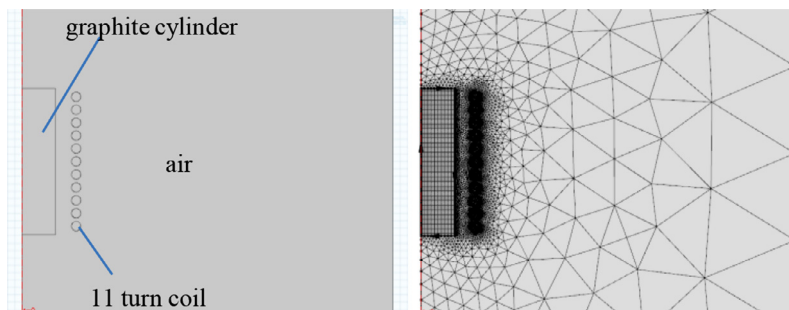


Fig. 3. The geometry used in the FEA to simulate the experimental setup (left), and the mesh used in the FEA (right). The mesh used for all of the results reported here consists of 8580 elements.

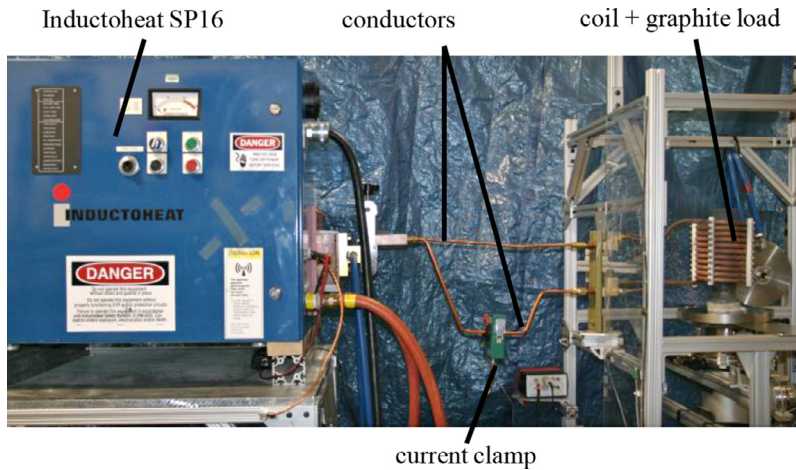


Fig. 4. Picture of the experimental setup showing the power supply, conductors, and the coil with graphite load.

temperature was measured using a Type K thermocouple embedded in a hole drilled 0.635 cm deep in the bottom center of the cylinder.

4.3. Input parameters and run-time for the analytical solution and FEA

Table 2 presents the input parameters used to evaluate the expressions in the analytical solution and the FEA. The geometry of the graphite used in both models is the same geometry that is used in the experiments. Values for graphite density and temperature dependent thermal conductivity, electrical conductivity, and specific heat are obtained from values reported for POCO AXM-5Q ultrafine grain graphite [20]. The FEA uses an induction coil with the same dimensions as the coil used in the experiments (dimensions listed above). In the analytical solution, we assume an 11 turn induction coil is used with the radius of the induction coil, b , equal to the inside radius of the induction coil used in the experiment. Both the analytical and FEA models assume an ambient temperature of 293.15 K and a constant surface emissivity of graphite equal to 0.9. The voltage across the tank circuit is set to 47.1 V (RMS), which is the voltage across the secondary winding of the isolation transformer assuming that the inverter supplies the maximum 400 V (RMS) to the primary. The current delivered to the tank circuit is set equal to the percent current set by the operator, $\%I$, times the maximum current available at the secondary of the isolation transformer. Finally, the capacitance in the tank circuit can be manually adjusted in the power supply. For the results reported here, we used two different settings in the capacitor bank, $C = 15.41 \mu\text{F}$ or $C = 55.7 \mu\text{F}$.

Table 2
Input parameters to evaluate the analytical and FEA solutions.

T_{∞}	293.15 K	I (RMS)	$\%I \cdot 1063$ A	
R	4.51 cm	V_{max} (RMS)	47.1 V	
b	6.65 cm	L_{cir}^C	0.87 μ H	
l	19.8 cm	C	15.41/55.7 μ F	
N	11	ε_R	0.9	
Properties of POCO graphite				
T (K)	σ (1/ Ω m)	c (J/kg K)	k (W/m K)	ρ (kg/m ³)
293.15	75,250	721	120	1720
393.15	86,417	1026	108	1720
493.15	96,585	1269	95	1720
593.15	105,001	1424	88	1720
693.15	111,244	1549	80	1720
793.15	115,292	1645	75	1720
893.15	117,437	1712	70	1720
993.15	118,124	1763	66	1720
1093.15	117,807	1809	62	1720
1193.15	116,860	1855	60	1720
1293.15	115,549	1892	57	1720
1393.15	114,035	1926	56	1720
1493.15	112,396	1959	55	1720

Table 3

Experiments performed.

Experiment #	C (μ F)	%I	ε_{max}	Comments
1	15.41	44	0.33	High frequency fast startup
2	15.41	26	0.32	High frequency slow startup
3	55.7	54	0.46	Low frequency fast startup
4	55.7	32	0.43	Low frequency slow startup

The analytical solution is programmed into and solved by a spreadsheet program. A total of 300 equally spaced time steps are used to evaluate the integral in the energy equation using the explicit integration scheme of Eq. (43).

Both the coupled multi-physics Comsol FEA model and the analytical solution were evaluated on a computer with dual 2 GHz 8 core processors with 16 GB of RAM and a 64 bit operating system. Transient simulations include the first 1500 s after startup. Typically, approximately 30 min of computer run-time is required to evaluate the first 1500 s of the transient solution using the FEA model. By comparison, the numerical integration in the analytical solution, which is evaluated in a spreadsheet program, requires less than 0.3 s of computer run-time to evaluate the first 1500 s of the transient solution.

4.4. Experiments performed

Four transient heating experiments were performed for heating of the graphite cylinder from ambient temperature to a temperature near 900 °C. In the experiments, the two different capacitor settings were used and either high or low current setting was used. Values for the capacitor bank setting and the current setting of the power supply are listed in Table 3 for each of the four experiments. The table also shows the maximum value reached by the perturbation parameter, ε_{max} , as calculated by the analytical solution for each of the experimental conditions. In all cases $\varepsilon < 0.5$. The two experiments with the highest current setting were used for a fast heat-up to 900 °C (typically <5 min), while the two experiments with lower current setting give a longer heat-up time (typically ~20 minutes to 900 °C). In the experiments with the lower value of C, the power supply frequency is near $f = 15$ kHz, whereas with the higher value of C the power supply frequency is near $f = 10$ kHz.

4.5. Comparisons between experiments and models

A comparison between the measured power supply frequency and the frequencies calculated with the analytical and FEA models for the conditions of experiment #1 is shown in Fig. 5. The calculated average temperature of the load from the analytical and FEA models and the thermocouple measurement are also shown in Fig. 5. The conditions for experiment #1 lead to a fast heat up to 900 °C in less than 5 min with the power supply operating at a relatively high frequency, ~80% of maximum output frequency.

Fig. 5 shows that both the FEA and analytical solution slightly (by less than 500 Hz) over-predict the power supply output frequency. However, the results show that both models do correctly predict that the output frequency rises during the initial portion of the heat-up, reaches a maximum frequency f_{max} at a time t_{max} then decreases as heating continues. The comparison for the average load temperature during warm-up shows that the analytical and FEA models agree to within 30 °C throughout warm-up. The measured temperature is significantly lower than the temperatures predicted by the models. In the experiment, however, the temperature is measured at the bottom center of the load. During this fast start-up, there is a significant temperature gradient between the heated zone and the bottom of the load. We will show that in the slower heating experiments (#2 and #4) the experimentally observed temperatures are much closer to those predicted by the models.

The small differences between the absolute level (or the f_{max}) of the output frequency from the analytical model, the FEA, and experiment are likely due to a number of factors including slight differences in material properties (electrical conductivity,

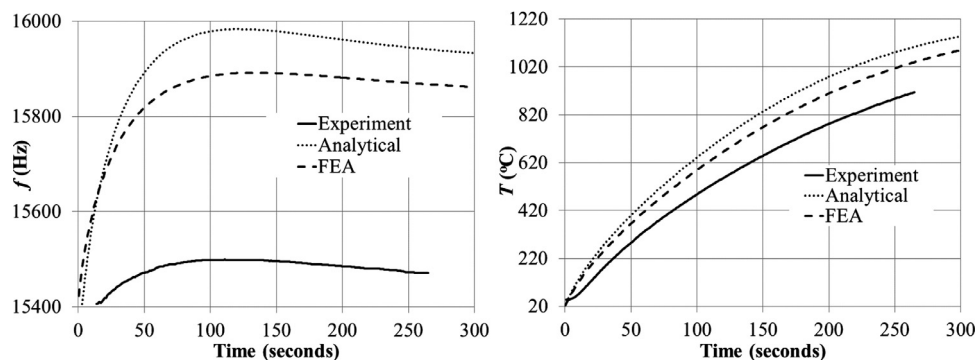


Fig. 5. Measured and calculated power supply frequency and load temperature during heating for the conditions of experiment #1.

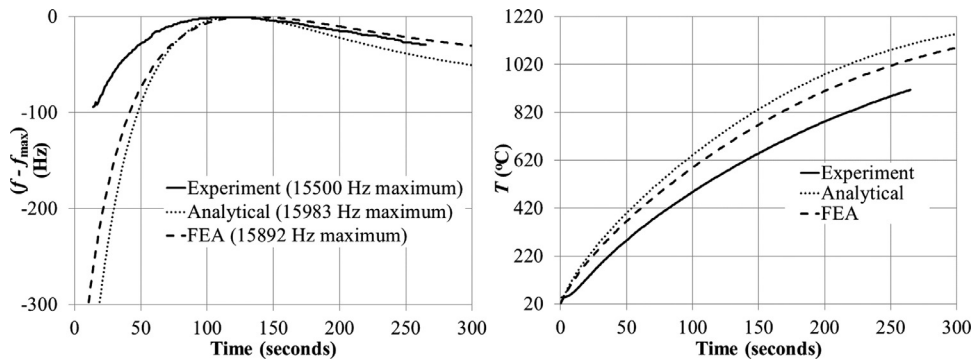


Fig. 6. The normalized power supply frequency and temperature from the experiment, analytical solution and FEA for the conditions of experiment #1. The maximum value of the frequency is reported in the legend.

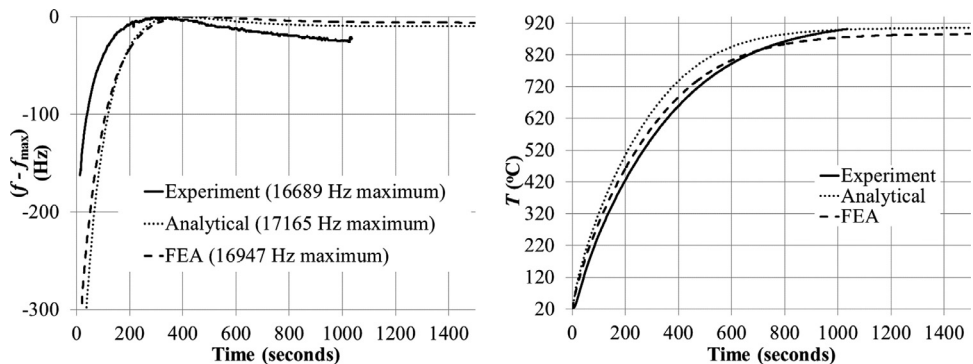


Fig. 7. The normalized power supply frequency and temperature from the experiment, analytical solution and FEA for the conditions of experiment #2. The maximum value of the frequency is reported in the legend.

surface emissivity) between experiment and models and the simplifying assumptions made in the development of the analytical solution. For instance, in developing the analytical solution, the current through the induction coil is approximated as a current sheet. Unlike the FEA and experiment, the model developed here ignores any flux leakage between turns of the coil.

Although there are small differences between the predicted and observed overall level of the output frequency, it is more important for load signature analysis to observe that for the FEA, the analytical model, and the experiment the overall shape of the predicted output frequency is the same. The output frequency of the power supply rises to a maximum value near 125 s after start-up then decreases slightly in the later part of the warm-up.

The predicted and experimentally observed shape of the power supply output frequency can be understood with the help of Eq. (51). The equation shows that the temperature and time dependence of the power supply output frequency are only due to the temperature dependence of the electrical conductivity of the load. Fig. 5 shows that for both the analytical and FEA models, the predicted average temperature of the load is near 720 °C at 125 s after start-up, where the frequency reaches f_{max} . Table 2 shows that the electrical conductivity of POCO graphite reaches a maximum at 720 °C (993.15 K). In this way, the observed output frequency of the power supply can be used to observe the temperature dependence of the properties of the material being heated.

As stated above, for load signature analysis we are most interested in the evolution of the frequency output over time. In Fig. 6, we normalize the output frequency by plotting $f - f_{max}$ throughout the heating event for the experimental, FEA, and analytical solutions. The figure shows that the time at which the maximum frequency occurs is accurately predicted by both the FEA and the analytical solution. Moreover, both models faithfully reproduce the shape of the response curve and correctly predict the magnitude of frequency changes during heating.

Plots of $f - f_{max}$ and the average load temperature for the conditions of experiments #2, #3, and #4 throughout heating are shown in Figs. 7, 8, and 9, respectively. The figures show that over the range of power supply settings used in the experiments the analytical solution correctly predicts the power supply output frequency changes and the temperature of the load. The plots also show that for the slow heating experiments (#2 and #4) the measured temperature of the load is close to the calculated temperatures.

Finally, Table 4 shows comparisons between experimentally measured values and values calculated by the analytical solution and the FEA for the maximum frequency, f_{max} , and the time at which the maximum frequency is reached, t_{max} . The parameters f_{max} and t_{max} are measures essential for characterizing the time evolution of the frequency response. Table 4 shows that the

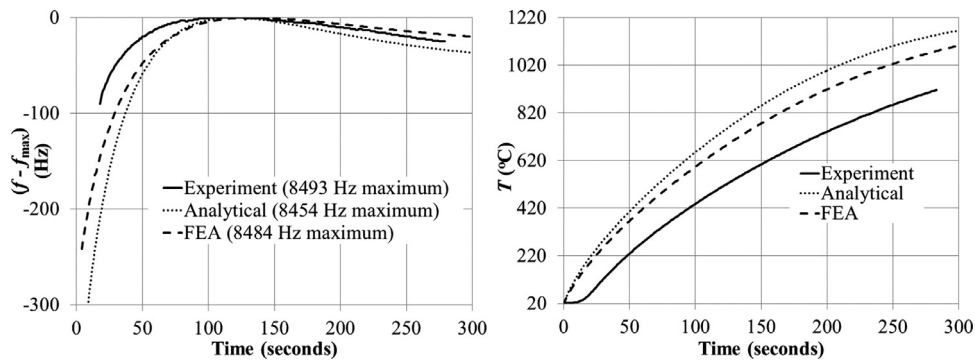


Fig. 8. The normalized power supply frequency and temperature from the experiment, analytical solution and FEA for the conditions of experiment #3. The maximum value of the frequency is reported in the legend.

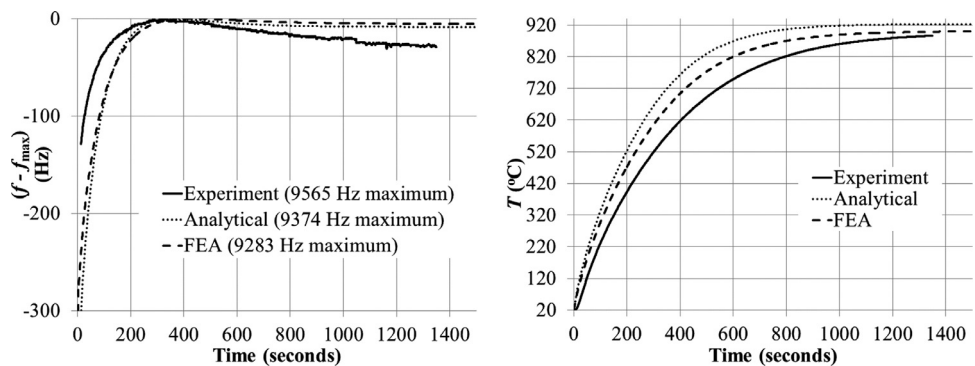


Fig. 9. The normalized power supply frequency and temperature from the experiment, analytical solution and FEA for the conditions of experiment #4. The maximum value of the frequency is reported in the legend.

Table 4

Comparisons between experimentally measured and calculated values for f_{max} and t_{max} for all four experiments performed.

Experiment #	f_{max} (Hz)			Relative error* (%)	
	Experimental	Analytical	FEA	Analytical	FEA
1	15,500	15,983	15,892	3.1	2.5
2	16,689	17,165	16,947	2.9	1.5
3	8493	8454	8484	−0.5	−0.1
4	9565	9374	9283	−2.0	−2.9
	t_{max} (s)			Relative error* (%)	
	Experimental	Analytical	FEA	Analytical	FEA
1	111	119	133	7.2	19.8
2	342	380	443	11.1	29.5
3	131	116	133	−11.5	1.5
4	329	355	422	7.9	28.3

* Error calculated relative to experimental values.

relative error between the analytical solution and the experimental measurements is less than 12% for all four experiments performed.

5. Conclusions

An approximate analytical solution for induction heating of non-magnetic cylinders by a cylindrical induction coil is presented. For the solution presented here, the induction coil is used in a series-tuned tank circuit and is excited by a variable frequency voltage-source power supply. The analytical solution allows for a prediction of the cylinder temperature and power supply frequency throughout heating.

Comparisons between the approximate analytical solution and FEA and experimental data show that the analytical solution is able to capture the frequency and temperature evolution during heating.

In the development of the approximate solution, the magnetic field in the heated material is determined from a perturbation analysis based on the multiple-scales method. Previous authors have used perturbation methods to approximate fields in induction heating applications [21]; however, the asymptotic solutions were used to simplify numerical simulations of complex geometries, never to give a complete description of the electromagnetic field in the heated object. To our knowledge, the multiple-scales solution presented here, which is shown to compare favorably to the exact solution and is a simple polynomial expression compared to the special functions needed to evaluate the exact solution, has not been formulated elsewhere. When expressions from the perturbation solution for the magnetic field are used to calculate the impedance of the tank circuit, the frequency response of the power supply can also be expressed as a relatively simple function of the power supply settings and material properties of the heated object. The simple expressions developed here are physics-based expressions that can be used to gain insight into the factors affecting observations from load signature analysis.

Acknowledgments

The authors thank Dr. Joseph Majdalani (Aerospace Engineering Department, Auburn University) for his review of the manuscript and for advice on implementation of the multiple-scale technique. Los Alamos National Laboratory, an affirmative action/equal opportunity employer, is operated by Los Alamos National Security, LLC, for the National Nuclear Security Administration of the U.S. Department of Energy under Contract [DE-AC52-06NA25396](#).

References

- [1] S. Zinn, S.L. Semiatin, *Elements of Induction Heating*, ASM International, Metals Park, OH, 1988.
- [2] J.D. Verhoeven, H.L. Downing, E.D. Gibson, Induction case hardening of steel, *J. Heat Treat.* 4 (3) (1986) 253–264.
- [3] F. Cajner, B. Smoljan, D. Landek, Computer simulation of induction hardening, *J. Mater. Process. Technol.* 157–158 (2004) 55–60.
- [4] J. Nerg, K. Tolsa, P. Silventoinen, J. Partanen, J. Pyrhonen, A dynamic model for the simulation of induction heating devices, *IEEE Trans. Magn.* 35 (5) (1999) 3592–3594.
- [5] Y. Ge, R. Hu, Z. Zhang, Q. Shen, Optimization control of induction hardening process, in: *Proceedings of IEEE International Conference on Mechatronics and Automation*, Luoyang, China, 2006.
- [6] H. Kagimoto, D. Miyagi, N. Takahashi, Effect of temperature dependence of magnetic properties on heating characteristics of induction heater, *IEEE Trans. Magn.* 46 (8) (2006) 3018–3021.
- [7] M. Blodt, Models for bearing damage detection in induction motors using stator current monitoring, *IEEE Trans. Ind. Electron.* 55 (4) (2008) 1813–1822.
- [8] C. Bruzzese, Analysis and application of particular current signatures (symptoms) for cage monitoring in nonsinusoidally fed motors with high rejection to drive load, inertia, and frequency variations, *IEEE Trans. Ind. Electron.* 55 (12) (2008) 4137–4155.
- [9] H. Henao, Wire rope fault detection in a hoisting winch system by motor torque and current signature analysis, *IEEE Trans. Ind. Electron.* 58 (5) (2011) 1727–1736.
- [10] S. Nandi, H.A. Toliyat, X. Li, Condition monitoring and fault diagnosis of electrical machines – a review, *IEEE Trans. Energy Convers.* 20 (4) (2005) 719–729.
- [11] E.J. Davies, *Conduction and Induction Heating*, Institution of Engineering and Technology, London, 1990.
- [12] M.W. Kennedy, S. Akhtar, J.A. Bakken, R.E. Aune, Empirical verification of a short-coil correction factor, *IEEE Trans. Ind. Electron.* 61 (5) (2014) 2573–2583.
- [13] R. Lundin, A handbook formula for the inductance of a single-layer circular coil, *Proc. IEEE* 73 (9) (1985) 1428–1429.
- [14] C.M. Bender, S.A. Orszag, *Advanced Mathematical Methods for Scientists and Engineers*, McGraw-Hill, New York, 1978.
- [15] E. Zok, D.M. Schibisch, Energy-efficient power supply for induction hardening and heating processes, *Induction Technology Reports*, No. 1, 2013, pp. 67–74.
- [16] F.W. Grover, *Inductance Calculations*, Van Nostrand, New York, 1946.
- [17] O. Bodart, A. Boureau, R. Touzani, Numerical investigation of optimal control of induction heating processes, *Appl. Math. Model.* 25 (2001) 697–712.
- [18] H. Kawaguchi, M. Enokizono, T. Todaka, Thermal and magnetic field analysis of induction heating problems, *J. Mater. Process. Technol.* 161 (2005) 193–198.
- [19] R. Naar, F. Bay, Numerical optimization for induction heat treatment processes, *Appl. Math. Model.* 37 (2013) 2074–2085.
- [20] *Properties and characteristics of graphite*, 4th ed., POCO Graphite Inc., Decatur, TX, 1994.
- [21] F. Bioul, F. Dupret, Application of asymptotic expansions to model two-dimensional induction heating systems. Part I: calculation of electromagnetic field distribution, *IEEE Trans. Magn.* 41 (9) (2005) 2496–2505.